

Chapter 2

Modeling of Thermal Non-equilibrium

2.1 Introduction

Convection heat transfer in porous media has been extensively investigated due to its many important engineering applications. The wide applications available have led to numerous investigations in this area. Such applications can be found in solar receiver devices, building thermal insulation, heat exchangers, energy storage units, etc. From the point of view of the energy equation there are two different models, local thermal equilibrium model and two energy approach. The first model assumes that the solid temperature is equal to the fluid temperature, thus local thermal equilibrium between the fluid and the solid-phases is achieved at any location in the porous media. This model simplifies theoretical and numerical research, but the assumption of local thermal equilibrium between the fluid and the solid is inadequate for a number of problems [1, 2]. In recent years more attention has been paid to the local thermal non-equilibrium model and its use has increased in theoretical and numerical research for convection heat transfer processes in porous media [3, 4]. Saito and de Lemos [5] considered local thermal non-equilibrium and obtained the interfacial heat transfer coefficient for laminar flow using a single unit cell with local instantaneous transport equations.

This chapter details the proposition of a new correlation for obtaining the interfacial heat transfer coefficient for turbulent flow in a packed bed. The bed is modeled as an infinite staggered array of square rods and the range of Reynolds number, based on the size of the rod, is extended up to 10^7 . In-line rod arrangement is here not considered as the objective of this work is first to consolidate results for staggered arrays. Future investigations shall consider different array arrangements as well as distinct rod shapes, such as elliptical and circular rods.

The next sessions details the basic mathematical model, including the mean and turbulent fields for turbulent flows. Although the discussion of turbulent motion in porous media isn't present in this work the definition and concept to calculating the interfacial heat transfer coefficient for macroscopic flows are presented.

2.2 Governing Equations

2.2.1 Local Instantaneous Transport Equations

Microscopic transport equations or local time-averaged transport equations for incompressible fluid flow in a rigid homogeneous porous medium have been already presented in the literature and for that, they are here just presented [6]. The governing equations for the flow and energy for an incompressible fluid are given by:

$$\text{Continuity: } \nabla \cdot \mathbf{u} = 0. \quad (2.1)$$

$$\text{Momentum: } \rho \left[\frac{\partial \mathbf{u}}{\partial t} + \nabla \cdot (\mathbf{u}\mathbf{u}) \right] = -\nabla p + \mu \nabla^2 \mathbf{u}. \quad (2.2)$$

$$\text{Energy-Fluid Phase: } (\rho c_p)_f \left\{ \frac{\partial T_f}{\partial t} + \nabla \cdot (\mathbf{u} T_f) \right\} = \nabla \cdot (k_f \nabla T_f) + S_f. \quad (2.3)$$

$$\text{Energy-Solid Phase(Porous Matrix) : } (\rho c_p)_s \frac{\partial T_s}{\partial t} = \nabla \cdot (k_s \nabla T_s) + S_s. \quad (2.4)$$

where the subscripts f and s refer to fluid and solid phases, respectively. Here, T is the temperature k_f is the fluid thermal conductivity, k_s is the solid thermal conductivity, c_p is the specific heat and S is the heat generation term. If there is no heat generation either in the solid or in the fluid, one has further $S_f = S_s = 0$.

For turbulent flows, the standard time averaged transport equations can be written as:

$$\text{Continuity: } \nabla \cdot \bar{\mathbf{u}} = 0. \quad (2.5)$$

$$\text{Momentum: } \rho_f [\nabla \cdot (\bar{\mathbf{u}}\bar{\mathbf{u}})] = -\nabla \bar{p} + \nabla \cdot \{ \mu [\nabla \bar{\mathbf{u}} + (\nabla \bar{\mathbf{u}})^T] - \rho \overline{\mathbf{u}'\mathbf{u}'} \}. \quad (2.6)$$

where the low and high Reynolds $k - \varepsilon$ model is used to obtain the eddy viscosity, μ_t , whose equations for the turbulent kinetic energy per unit mass and for its dissipation rate read:

Turbulent kinetic energy per unit mass:

$$\rho_f [\nabla \cdot (\bar{\mathbf{u}}k)] = \nabla \cdot \left[\left(\mu + \frac{\mu_t}{\sigma_k} \right) \nabla k \right] - \rho \overline{\mathbf{u}'\mathbf{u}'} : \nabla \bar{\mathbf{u}} - \rho \varepsilon \quad (2.7)$$

Turbulent kinetic energy per unit mass dissipation rate:

$$\rho_f [\nabla \cdot (\bar{\mathbf{u}}\varepsilon)] = \nabla \cdot \left[\left(\mu + \frac{\mu_t}{\sigma_\varepsilon} \right) \nabla \varepsilon \right] + [c_1 (-\rho \overline{\mathbf{u}'\mathbf{u}'} : \nabla \bar{\mathbf{u}}) - c_2 f_2 \rho \varepsilon] \frac{\varepsilon}{k} \quad (2.8)$$

Reynolds stresses and the Eddy viscosity is given by, respectively:

$$-\rho \overline{\mathbf{u}'\mathbf{u}'} = \mu_t [\nabla \bar{\mathbf{u}} + (\nabla \bar{\mathbf{u}})^T] - \frac{2}{3} \rho k \mathbf{I} \quad (2.9)$$

$$\mu_t = \rho c_\mu f_\mu \frac{k^2}{\varepsilon} \quad (2.10)$$

where, ρ is the fluid density, p is the pressure, μ represents the fluid viscosity.

In the above equation set σ_k , σ_ε , c_1 , c_2 , and c_μ are dimensionless constants whereas f_2 and f_μ are damping functions of the low Re $k - \varepsilon$ turbulence models is justified by the fact that the turbulent flow in porous media occurs for Reynolds number relatively low. To account for the low Reynolds effects, the following damping functions were adopted.

$$f_\mu = \left\{ 1 - \exp \left[-\frac{(v\varepsilon)^{0.25} y}{14 v} \right] \right\}^2 \left\{ 1 + \frac{5}{(k^2/v\varepsilon)^{0.75}} \exp \left[-\left(\frac{k^2/v\varepsilon}{200} \right)^2 \right] \right\} \quad (2.11)$$

$$f_2 = \left\{ 1 - \exp \left[-\frac{(v\varepsilon)^{0.25} y}{3.1 v} \right] \right\}^2 \left\{ 1 - 0.3 \exp \left[-\left(\frac{k^2/v\varepsilon}{6.5} \right)^2 \right] \right\} \quad (2.12)$$

where y is the coordinate normal to the wall. The turbulent model constants are given as follows,

$$c_\mu = 0.09, c_1 = 1.5, c_2 = 1.9, \sigma_k = 1.4, \sigma_\varepsilon = 1.3.$$

For the high Re model the standard constants of Launder and Spalding [7] were employed.

Also, the time averaged energy equations become:

$$\text{Energy-Fluid Phase: } (\rho c_p)_f [\nabla \cdot (\bar{\mathbf{u}} \bar{T}_f)] = \nabla \cdot (k_f \nabla \bar{T}_f) - (\rho c_p)_f \nabla \cdot (\overline{\mathbf{u}' T'_f}). \quad (2.13)$$

$$\text{Energy-Solid Phase (Porous Matrix): } \nabla \cdot (k_s \nabla \bar{T}_s) + S_s = 0. \quad (2.14)$$

2.2.2 Double-Decomposition of Variables

Macroscopic transport equations for turbulent flow in a porous medium are obtained through the simultaneous application of time and volume average operators over a generic fluid property φ . Such concepts are defined as [8–10].

$$\bar{\varphi} = \frac{1}{\Delta t} \int_t^{t+\Delta t} \varphi dt, \quad \text{with} \quad \varphi = \bar{\varphi} + \varphi' \quad (2.15)$$

for time splitting, as used in Eqs. (2.14)–(2.22), and

$$\langle \varphi \rangle^i = \frac{1}{\Delta V_f} \int_{\Delta V_f} \varphi dV; \quad \langle \varphi \rangle^v = \phi \langle \varphi \rangle^i; \quad \phi = \frac{\Delta V_f}{\Delta V}, \quad \text{with} \quad \varphi = \langle \varphi \rangle^i + {}^i\varphi \quad (2.16)$$

for volume splitting, where ΔV_f is the volume of the fluid contained in a Representative Elementary Volume ΔV (REV, see Fig. 1.2a). Intrinsic average (fluid-based) and volume average (fluid-plus-solid-based) are represented, respectively, by $\langle \rangle^i$ and $\langle \rangle^v$. The double decomposition idea, introduced and fully described in [8–10], combines Eqs. (2.15) and (2.16) and can be summarized as:

$$\overline{\langle \varphi \rangle^i} = \langle \bar{\varphi} \rangle^i; \quad {}^i\bar{\varphi} = \overline{{}^i\varphi}; \quad \langle \varphi' \rangle^i = \langle \varphi \rangle^{i'} \quad (2.17)$$

and,

$$\left. \begin{array}{l} \varphi' = \langle \varphi' \rangle^i + {}^i\varphi' \\ {}^i\varphi = \overline{{}^i\varphi} + {}^i\varphi' \end{array} \right\} \quad \text{where} \quad {}^i\varphi' = \varphi' - \langle \varphi' \rangle^i = {}^i\varphi - \overline{{}^i\varphi} \quad (2.18)$$

therefore, the general vector quantity φ can be expressed by either,

$$\varphi = \overline{\langle \varphi \rangle^i} + \langle \varphi \rangle^{i'} + \overline{{}^i\varphi} + {}^i\varphi' \quad (2.19)$$

or

$$\varphi = \langle \bar{\varphi} \rangle^i + {}^i\bar{\varphi} + \langle \varphi' \rangle^i + {}^i\varphi'. \quad (2.20)$$

The term ${}^i\varphi'$ can be viewed as either the temporal fluctuation of the spatial deviation or the spatial deviation of the temporal fluctuation of the quantity φ .

2.2.3 Macroscopic Flow Equations

When the average operators (2.15) and (2.16) are simultaneously applied over Eqs. (2.1) and (2.2), macroscopic equations for turbulent flow are obtained. Volume integration is performed over a Representative Elementary Volume (REV) [11, 12], resulting in,

$$\text{Continuity: } \nabla \cdot \bar{\mathbf{u}}_D = 0. \quad (2.21)$$

where, $\bar{\mathbf{u}}_D = \phi \langle \bar{\mathbf{u}} \rangle^i$ and $\langle \bar{\mathbf{u}} \rangle^i$ identifies the intrinsic average of the time-averaged velocity vector $\bar{\mathbf{u}}$.

Momentum:

$$\begin{aligned} \rho \left[\frac{\partial \bar{\mathbf{u}}_D}{\partial t} + \nabla \cdot \left(\frac{\bar{\mathbf{u}}_D \bar{\mathbf{u}}_D}{\phi} \right) \right] = & -\nabla(\phi \langle \bar{p} \rangle^i) + \mu \nabla^2 \bar{\mathbf{u}}_D - \nabla \cdot (\rho \phi \langle \bar{\mathbf{u}}' \bar{\mathbf{u}}' \rangle^i) \\ & - \left[\frac{\mu \phi}{K} \bar{\mathbf{u}}_D + \frac{c_F \phi \rho |\bar{\mathbf{u}}_D| \bar{\mathbf{u}}_D}{\sqrt{K}} \right] \end{aligned} \quad (2.22)$$

where the last two terms in Eq. (2.2) represent the Darcy and Forchheimer or form drags. The symbol K is the porous medium permeability, c_F is the form drag or Forchheimer coefficient, $\langle \bar{p} \rangle^i$ is the intrinsic average pressure of the fluid and ϕ is the porosity of the porous medium.

The macroscopic Reynolds stress, $-\rho \phi \langle \bar{\mathbf{u}}' \bar{\mathbf{u}}' \rangle^i$, appearing in Eq. (2.22) is given as,

$$-\rho \phi \langle \bar{\mathbf{u}}' \bar{\mathbf{u}}' \rangle^i = \mu_{t_\phi} 2 \langle \bar{\mathbf{D}} \rangle^v - \frac{2}{3} \phi \rho \langle k \rangle^i \mathbf{I} \quad (2.23)$$

where,

$$\langle \bar{\mathbf{D}} \rangle^v = \frac{1}{2} [\nabla(\phi \langle \bar{\mathbf{u}} \rangle^i) + [\nabla(\phi \langle \bar{\mathbf{u}} \rangle^i)]^T] \quad (2.24)$$

is the macroscopic deformation tensor, $\langle k \rangle^i = \langle \bar{\mathbf{u}}' \cdot \bar{\mathbf{u}}' \rangle^i / 2$ is the macroscopic turbulent kinetic energy, and μ_{t_ϕ} , is the turbulent viscosity, which is modeled in [9] similarly to the case of clear flow, in the form,

$$\mu_{t_\phi} = \rho c_\mu \frac{\langle k \rangle^i}{\langle \varepsilon \rangle^i} \quad (2.25)$$

The intrinsic turbulent kinetic energy per unit mass and its dissipation rate are governed by the following equations,

$$\begin{aligned} \rho \left[\frac{\partial}{\partial t} (\phi \langle k \rangle^i) + \nabla \cdot (\bar{\mathbf{u}}_D \langle k \rangle^i) \right] = & \nabla \cdot \left[\left(\mu + \frac{\mu_{t_\phi}}{\sigma_k} \right) \nabla (\phi \langle k \rangle^i) \right] - \rho \langle \bar{\mathbf{u}}' \bar{\mathbf{u}}' \rangle^i : \nabla \bar{\mathbf{u}}_D \\ & + c_k \rho \frac{\phi \langle k \rangle^i |\bar{\mathbf{u}}_D|}{\sqrt{K}} - \rho \phi \langle \varepsilon \rangle^i \end{aligned} \quad (2.26)$$

$$\begin{aligned}
\rho \left[\frac{\partial}{\partial t} (\phi \langle \varepsilon \rangle^i) + \nabla \cdot (\bar{\mathbf{u}}_D \langle \varepsilon \rangle^i) \right] &= \nabla \cdot \left[\left(\mu + \frac{\mu_\phi}{\sigma_\varepsilon} \right) \nabla (\phi \langle \varepsilon \rangle^i) \right] + c_1 (-\rho \langle \bar{\mathbf{u}}' \mathbf{u}' \rangle^i : \nabla \bar{\mathbf{u}}_D) \frac{\langle \varepsilon \rangle^i}{\langle k \rangle^i} \\
&\quad + c_2 c_k \rho \frac{\phi \langle \varepsilon \rangle^i |\bar{\mathbf{u}}_D|}{\sqrt{K}} - c_2 \rho \phi \frac{\langle \varepsilon \rangle^{i^2}}{\langle k \rangle^i}
\end{aligned} \tag{2.27}$$

where, $\sigma_k = 1$, $\sigma_\varepsilon = 1.3$, $c_1 = 1.44$, $c_2 = 1.92$, $c_\mu = 0.09$ and $c_k = 0.28$ are non-dimensional constants [8–10].

2.2.4 Macroscopic Energy Equations

Similarly, macroscopic energy equations are obtained for both fluid and solid phases by applying time and volume average operators to Eqs. (2.3) and (2.4). As in the flow case, volume integration is performed over a Representative Elementary Volume (REV), resulting in,

$$\begin{aligned}
(\rho c_p)_f \left[\frac{\partial \phi \langle \bar{T}_f \rangle^i}{\partial t} + \nabla \cdot \left\{ \phi \left(\langle \bar{\mathbf{u}} \rangle^i \langle \bar{T}_f \rangle^i + \underbrace{\langle \bar{\mathbf{u}}' \bar{T}_f' \rangle^i}_{\text{thermal dispersion}} + \underbrace{\langle \bar{\mathbf{u}}' \rangle^i \langle \bar{T}_f' \rangle^i}_{\text{turbulent heat flux}} + \underbrace{\langle \bar{\mathbf{u}}' \rangle^i \langle \bar{T}_f' \rangle^i}_{\text{turbulent thermal dispersion}} \right) \right\} \right] \\
= \underbrace{\nabla \cdot \left[k_f \nabla (\phi \langle \bar{T}_f \rangle^i) + \frac{1}{\Delta V} \int_{A_i} \mathbf{n}_i k_f \bar{T}_f dA \right]}_{\text{conduction}} + \underbrace{\frac{1}{\Delta V} \int_{A_i} \mathbf{n}_i \cdot k_f \nabla \bar{T}_f dA}_{\text{interfacial heat transfer}}
\end{aligned} \tag{2.28}$$

where the expansion,

$$\langle \bar{\mathbf{u}}' \bar{T}_f' \rangle^i = \overline{\langle \langle \bar{\mathbf{u}}' \rangle^i + \bar{\mathbf{u}}' \rangle (\langle \bar{T}_f' \rangle^i + \bar{T}_f')}^i = \overline{\langle \bar{\mathbf{u}}' \rangle^i \langle \bar{T}_f' \rangle^i} + \overline{\langle \bar{\mathbf{u}}' \rangle^i \bar{T}_f'}^i \tag{2.29}$$

has been used in light of the double decomposition concept given by Eqs. (2.17)–(2.20) [8]. For the solid phase, one has,

$$\begin{aligned}
(\rho c_p)_s \left\{ \frac{\partial(1-\phi)\langle \bar{T}_s \rangle^i}{\partial t} \right\} = & \underbrace{\nabla \cdot \left\{ k_s \nabla [(1-\phi)\langle \bar{T}_s \rangle^i] - \frac{1}{\Delta V} \int_{A_i} \mathbf{n}_i k_s \bar{T}_s dA \right\}}_{\text{conduction}} \\
& - \underbrace{\frac{1}{\Delta V} \int_{A_i} \mathbf{n}_i \cdot k_s \nabla \bar{T}_s dA}_{\text{interfacial heat transfer}}
\end{aligned} \quad (2.30)$$

In (2.28) and (2.30), $\langle \bar{T}_s \rangle^i$ and $\langle \bar{T}_f \rangle^i$ denote the intrinsic average temperature of solid and fluid phases, respectively, A_i is the interfacial area within the REV and \mathbf{n}_i is the unit vector normal to the fluid-solid interface, pointing from the fluid towards the solid phase. Equations (2.28) and (2.30) are the macroscopic energy equations for the fluid and the porous matrix (solid), respectively.

In order to use Eqs. (2.28) and (2.30), the underscored terms have to be modeled in some way as a function of the intrinsically averaged temperature of solid phase and fluid, $\langle \bar{T}_s \rangle^i$ and $\langle \bar{T}_f \rangle^i$. To accomplish this, a gradient type diffusion model is used for all the terms, in the form,

$$\text{Turbulent heat flux: } -(\rho c_p)_f (\phi \overline{\langle \mathbf{u}' \rangle^i \langle T_f' \rangle^i}) = \mathbf{K}_t \cdot \nabla \langle \bar{T}_f \rangle^i. \quad (2.31)$$

$$\text{Thermal dispersion: } -(\rho c_p)_f (\phi \langle \mathbf{u}^i \bar{T}_f \rangle^i) = \mathbf{K}_{disp} \cdot \nabla \langle \bar{T}_f \rangle^i. \quad (2.32)$$

$$\text{Turbulent thermal dispersion: } -(\rho c_p)_f (\phi \overline{\langle \mathbf{u}^i T_f' \rangle^i}) = \mathbf{K}_{disp,t} \cdot \nabla \langle \bar{T}_f \rangle^i. \quad (2.33)$$

$$\text{Local conduction: } \begin{cases} \nabla \cdot \left[\frac{1}{\Delta V} \int_{A_i} \mathbf{n}_i k_f \bar{T}_f dA \right] = \mathbf{K}_{f,s} \cdot \nabla \langle \bar{T}_s \rangle^i \\ -\nabla \cdot \left[\frac{1}{\Delta V} \int_{A_i} \mathbf{n}_i k_s \bar{T}_s dA \right] = \mathbf{K}_{s,f} \cdot \nabla \langle \bar{T}_f \rangle^i \end{cases}. \quad (2.34)$$

where \mathbf{n}_i in (2.34), as mentioned, is the unit vector pointing outwards of the fluid phase. In this work, for simplicity, one assumes that for turbulent flow the overall thermal resistance between the two phases is controlled by the interfacial film coefficient rather than by the thermal resistance within each phase. As such, the coefficients $\mathbf{K}_{f,s}$, $\mathbf{K}_{s,f}$ are here neglected for the sake of simplicity. More information on such quantities is given below.

The heat transferred between the two phases can be modeled by means of a film coefficient h_i such that,

$$h_i a_i (\langle \bar{T}_s \rangle^i - \langle \bar{T}_f \rangle^i) = \frac{1}{\Delta V} \int_{A_i} \mathbf{n}_i \cdot k_f \nabla \bar{T}_f dA = \frac{1}{\Delta V} \int_{A_i} \mathbf{n}_i \cdot k_s \nabla \bar{T}_s dA. \quad (2.35)$$

where $a_i = A_i / \Delta V$ is the surface area per unit volume. Using the above shown expressions, Eqs. (2.28) and (2.30) can be written as:

$$\left\{ (\rho c_p)_f \phi \right\} \frac{\partial \langle \bar{T} \rangle^i}{\partial t} + (\rho c_p)_f \nabla \cdot (\mathbf{u}_D \langle \bar{T}_f \rangle^i) = \nabla \cdot \{ \mathbf{K}_{eff,f} \cdot \nabla \langle \bar{T}_f \rangle^i \} + h_i a_i (\langle \bar{T}_s \rangle^i - \langle \bar{T}_f \rangle^i), \quad (2.36)$$

$$\left\{ (1 - \phi) (\rho c_p)_s \right\} \frac{\partial \langle \bar{T}_s \rangle^i}{\partial t} = \nabla \cdot \{ \mathbf{K}_{eff,s} \cdot \nabla \langle \bar{T}_s \rangle^i \} - h_i a_i (\langle \bar{T}_s \rangle^i - \langle \bar{T}_f \rangle^i), \quad (2.37)$$

where, $\mathbf{K}_{eff,f}$ and $\mathbf{K}_{eff,s}$ are the effective conductivity tensor for fluid and solid, respectively, given by:

$$\mathbf{K}_{eff,f} = [\phi k_f] \mathbf{I} + \mathbf{K}_{f,s} + \mathbf{K}_t + \mathbf{K}_{disp} + \mathbf{K}_{disp,t}, \quad (2.38)$$

$$\mathbf{K}_{eff,s} = [(1 - \phi) k_s] \mathbf{I} + \mathbf{K}_{s,f}, \quad (2.39)$$

and \mathbf{I} is the unit tensor.

In order to be able to apply Eq. (2.36), it is necessary to determine the dispersion and conductivity tensors in Eq. (2.38), i.e., $\mathbf{K}_{f,s}$, \mathbf{K}_t , \mathbf{K}_{disp} and $\mathbf{K}_{disp,t}$. Following Kuwahara et al. [13] and Quintard et al. [3], $\mathbf{K}_{f,s}$ and \mathbf{K}_{disp} , are obtained by making use of a unit cell subjected to periodic boundary conditions, where (2.32) are (2.34) are numerically resolved. Further, dispersion tensor components are then obtained directly from the microscopic results, for a unit cell, and reads for $Pe_D \geq 10$ [13]:

$$\frac{(K_{disp})_{yy}}{k_f} = 0.052(1 - \phi)^{0.5} Pe_D, \text{ for transverse dispersion,} \quad (2.40)$$

$$\frac{(K_{disp})_{xx}}{k_f} = 2.1 \frac{Pe_D}{(1 - \phi)^{0.1}}, \text{ for longitudinal dispersion,} \quad (2.41)$$

Also, starting out from the time averaged energy equation, coupled with the microscopic modeling for the turbulent heat flux through the microscopic Eddy diffusivity, one can write:

$$-(\rho c_p)_f \overline{\mathbf{u}' T'_f} = (\rho c_p)_f \frac{v_t}{\sigma_T} \nabla \bar{T}_f \quad (2.42)$$

where σ_T is the turbulent Prandtl number which is taken here as a constant. Applying the volume average to the resulting Eq. (2.42) one obtains the macroscopic turbulent heat flux modeled as,

$$-(\rho c_p)_f \langle \mathbf{u}' T_f' \rangle^i = (\rho c_p)_f \frac{v_{t_\phi}}{\sigma_T} \nabla \langle T_f \rangle^i \quad (2.43)$$

where we have adopted the symbol v_{t_ϕ} to express the macroscopic version of the Eddy viscosity, $\mu_{t_\phi} = \rho_f v_{t_\phi}$.

Equation (2.43) represents the sum of the turbulent heat flux and the turbulent thermal dispersion terms. As such, the turbulent heat flux and turbulent thermal dispersion components of the conductivity tensor in Eq. (2.38), \mathbf{K}_t and $\mathbf{K}_{disp,t}$, which can not be determined from such a microscopic calculation, are here modeled through the Eddy diffusivity concept, as:

$$\mathbf{K}_t + \mathbf{K}_{disp,t} = \phi (\rho c_p)_f \frac{v_{t_\phi}}{\sigma_T} \mathbf{I} \quad (2.44)$$

where $\sigma_T = 0.9$ is the macroscopic turbulent Prandtl number for the fluid energy equation.

2.2.5 Correlations for Interfacial Heat Transfer, h_i

Wakao et al. [14] proposed a correlation for h_i for closely packed bed and compared results with their experimental data. This correlation reads,

$$\frac{h_i D}{k_f} = 2 + 1.1 Re_D^{0.6} Pr^{1/3}. \quad (2.45)$$

Kuwahara et al. [15] also obtained the interfacial convective heat transfer coefficient for laminar flow, as follows,

$$\frac{h_i D}{k_f} = \left(1 + \frac{4(1-\phi)}{\phi} \right) + \frac{1}{2} (1-\phi)^{1/2} Re_D Pr^{1/3}, \text{ valid for } 0.2 < \phi < 0.9, \quad (2.46)$$

Equation (2.46) is based on porosity dependency and is valid for packed beds of particle diameter D .

As will be seen below, in this work an additional correlation will be presented, which will be valid for both laminar and turbulent flows.

2.3 Periodic Cell

Nakayama et al. [16] and Kuwahara et al. [15] modeled a porous medium in terms of obstacles arranged in a regular pattern and solved the set of the local governing equations exploiting periodic boundary conditions. As such, consider a macroscopically uniform flow through an infinite number of square rods of lateral size D , placed in a staggered arrangement and maintained at constant temperature T_w . The periodic cell or representative elementary volume, ΔV , is schematically showed in Fig. 2.1a and has dimensions $2H \times H$. Computations within this cell were carried out using a non-uniform grid, as shown in Fig. 2.1b, to ensure that the results were grid independent. The Reynolds number $Re_D = \rho \bar{u}_D D / \mu$ was varied from 10^4 to 10^7 and the porosity was determined as $\phi = 1 - (D/H)^2$.

2.3.1 Numerical Method and Boundary Conditions

The numerical method utilized to discretize the flow and energy equations in the unit cell is the Finite Control Volume approach. The SIMPLE method of Patankar [17] was used for solving Eqs. (2.1)–(2.4) and for handling the velocity- pressure coupling. Convergence was monitored in terms of the normalized residue for each variable. The maximum residue allowed for convergence check was set to 10^{-9} , being the variables normalized by appropriate reference values.

For periodic fully developed flow in the cell of Fig. 2.1b, the velocity at exit ($x/H = 2$) must be identical to that at the inlet ($x/H = 0$). Temperature profiles, however, are only identical at both cell exit and inlet if presented in terms of an appropriate non-dimensional variable. The situation is analogous to the case of forced convection in a channel with isothermal walls. Due to the periodicity of the model a single structural unit, as depicted in Fig. 2.1b, may be taken as a calculation domain. The equations used for turbulent flow in the unit cell are Eqs. (2.5)–(2.14).

Thus, boundary conditions and periodic constraints are given by:

On the solid walls (Low Re):

$$\bar{u} = 0, k = 0, \quad \varepsilon = \nu \frac{\partial^2 k}{\partial y^2}, \quad \bar{T} = \bar{T}_w, \quad (2.47)$$

On the solid walls (high Re):

$$\frac{\bar{u}}{u_\tau} = \frac{1}{\kappa} \ln(y^+ E), \quad k = \frac{u_\tau^2}{c_\mu^{1/2}}, \quad \varepsilon = \frac{c_\mu^{3/4} k_w^{3/2}}{\kappa y_w}, \quad q_w = \frac{(\rho c_p)_f c_\mu^{1/4} k_w^{1/2} (\bar{T} - T_w)}{\left(\frac{Pr}{\kappa} \ln(y_w^+) + c_Q(Pr) \right)} \quad (2.48)$$

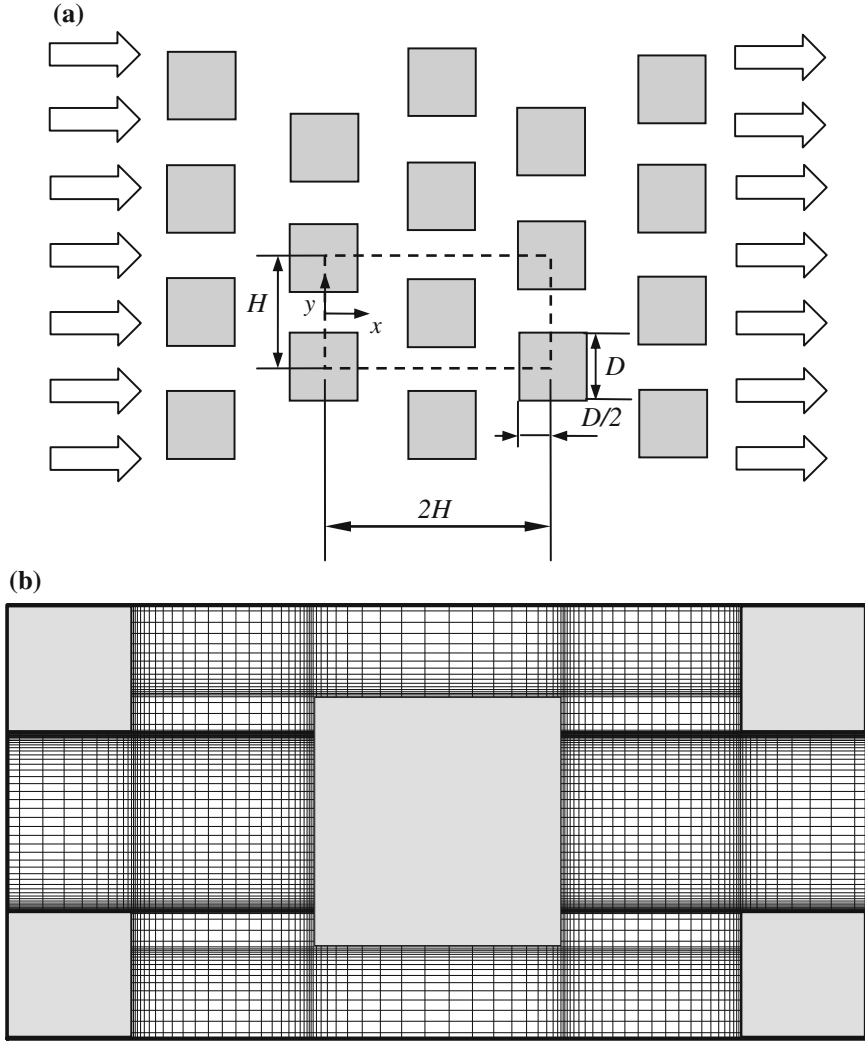


Fig. 2.1 Infinite medium: **a** Physical model and coordinate system, **b** Non uniform computational grid

where, $u_\tau = \left(\frac{\tau_w}{\rho}\right)^{1/2}$, $y_w^+ = \frac{y_w u_\tau}{\nu}$, $c_Q = 12.5Pr^{2/3} + 2.12 \ln(Pr) - 5.3$ for $Pr > 0.5$ where, Pr and Pr_t are Prandtl and turbulent Prandtl number, respectively, q_w is wall heat flux, u_τ is wall-friction velocity, y_w is the coordinate normal to wall, κ is constant for turbulent flow past smooth impermeable walls or von Kármán's constant and E is an integration constant that depends on the roughness of the wall. For smooth walls with constant shear stress $E = 9$.

On the symmetry planes:

$$\frac{\partial \bar{u}}{\partial y} = \frac{\partial \bar{v}}{\partial y} = \frac{\partial k}{\partial y} = \frac{\partial \varepsilon}{\partial y} = 0, \quad (2.49)$$

where \bar{u} and \bar{v} are components of $\bar{\mathbf{u}}$.

On the periodic boundaries:

$$\bar{u}|_{inlet} = \bar{u}|_{outlet}, \quad \bar{v}|_{inlet} = \bar{v}|_{outlet}, \quad k|_{inlet} = k|_{outlet}, \quad \varepsilon|_{inlet} = \varepsilon|_{outlet}, \quad (2.50)$$

$$\theta|_{inlet} = \theta|_{outlet} \Leftrightarrow \left. \frac{\bar{T} - \bar{T}_w}{\bar{T}_B(x) - \bar{T}_w} \right|_{inlet} = \left. \frac{\bar{T} - \bar{T}_w}{\bar{T}_B(x) - \bar{T}_w} \right|_{outlet}, \quad (2.51)$$

The bulk mean temperature of the fluid is given by:

$$\bar{T}_B(x) = \frac{\int \bar{u} \bar{T} dy}{\int \bar{u} dy} \quad (2.52)$$

Computations are based on the Darcy velocity, the length of structural unit H and the temperature difference $(\bar{T}_B(x) - \bar{T}_w)$, as references scales.

2.3.2 Film Coefficient H_i

Determination of h_i is here obtained by calculating, for the unit cell of Fig. 2.1b, an expression given as,

$$h_i = \frac{Q_{total}}{A_i \Delta T_{ml}} \quad (2.53)$$

where $A_i = 8D \times 1$. The overall heat transferred in the cell, Q_{total} , is giving by,

$$Q_{total} = (H - D) \rho \bar{u}_B c_p (\bar{T}_B|_{outlet} - \bar{T}_B|_{inlet}), \quad (2.54)$$

The bulk mean velocity of the fluid is given by:

$$\bar{u}_B(x) = \frac{\int \bar{u} dy}{\int dy} \quad (2.55)$$

and the logarithm mean temperature difference, ΔT_{ml} is,

$$\Delta T_{ml} = \frac{(\bar{T}_w - \bar{T}_B|_{outlet}) - (\bar{T}_w - \bar{T}_B|_{inlet})}{\ln[(\bar{T}_w - \bar{T}_B|_{outlet})(\bar{T}_w - \bar{T}_B|_{inlet})]} \quad (2.56)$$

Equation (2.54) represents an overall heat balance on the entire cell and associates the heat transferred to the fluid to a suitable temperature difference ΔT_{mt} . As mentioned earlier, Eqs. (2.1)–(2.4) were numerically solved in the unit cell until conditions Eqs. (2.50) and (2.51) were satisfied.

2.3.3 A Correlation for Interstitial Heat Transfer

Figure 2.2a show distributions of pressure, isotherms and turbulence kinetic energy in a microscopic porous structure, obtained at $Re_D = 10^5$ for cases of $\phi = 0.65$. Pressure increases at the front face of the square rod and drastically decreases around the corner, as can be seen from the pressure contours shown in Fig. 2.2a.

Temperature distribution is shown in Fig. 2.2b. Colder fluid impinges on the rod left side yielding strong temperature gradients on that face. Downstream the obstacles, fluid recirculation smooths temperature gradients and deforms isotherms within the mixing region. When the Reynolds number is sufficiently high (not shown here), thermal boundary layers cover the rod surfaces indicating that convective heat transfer overwhelms thermal diffusion. Figure 2.2c presents levels of turbulence kinetic energy, which are higher around the rod corners where a strong shear layer is formed. Further downstream the rods in the weak region, steep velocity gradients appear due to flow deceleration, increasing there also the local level of k .

Once fully developed flow and temperature fields are achieved, for the fully developed condition ($x > 6H$), bulk temperatures were calculated according to Eq. (2.52), at both inlet and outlet positions. They were then used to calculate h_i using Eqs. (2.53)–(2.56). Results for h_i are plotted in Fig. 2.3a for Re_D up to 10^7 . Also plotted in this figure are results computed with correlation (2.46) by Kuwahara et al. [15] using $\phi = 0.65$. The figure seems to indicate that both computations show a reasonable agreement for laminar results. In addition, numerical results for turbulent flow using Low and High Re models are also presented in this figure.

Figure 2.3b shows numerical results for the interfacial convective heat transfer coefficient for various porosities ($\phi = 0.44$, $\phi = 0.65$ and $\phi = 0.90$). Results for h_i are plotted for Re_D up to 10^7 . In order to obtain a correlation for h_i in the turbulent regime, all curves were first collapsed after plotting them in terms of Re_D/ϕ , as showed in Fig. 2.4a. Furthermore, the least square technique was applied in order to determine the best correlation, which lead to a minimum overall error. Thus, the following expression is here proposed:

$$\frac{h_i D}{k_f} = 0.08 \left(\frac{Re_D}{\phi} \right)^{0.8} Pr^{1/3}; \quad \text{for } 1.0 \times 10^4 < \frac{Re_D}{\phi} < 2.0 \times 10^7, \quad (2.57)$$

valid for $0.2 < \phi < 0.9$,

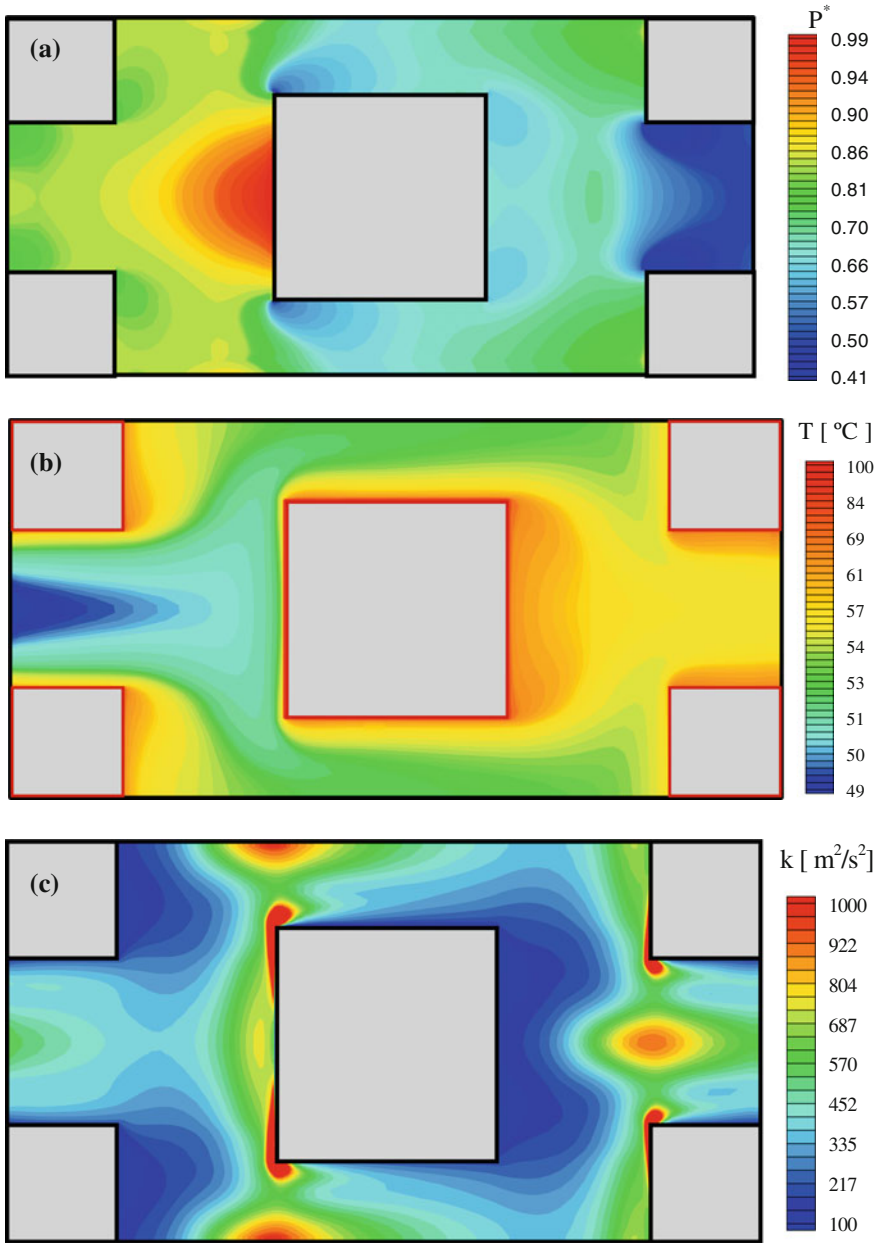


Fig. 2.2 Results for periodic cell: **a** Nondimensional pressure field for $Re_D = 10^5$ and $\phi = 0.65$, **b** Isotherms for $Pr = 1$, $Re_D = 10^5$ and $\phi = 0.65$, **c** Turbulence kinetic energy for $Re_D = 10^5$ and $\phi = 0.65$

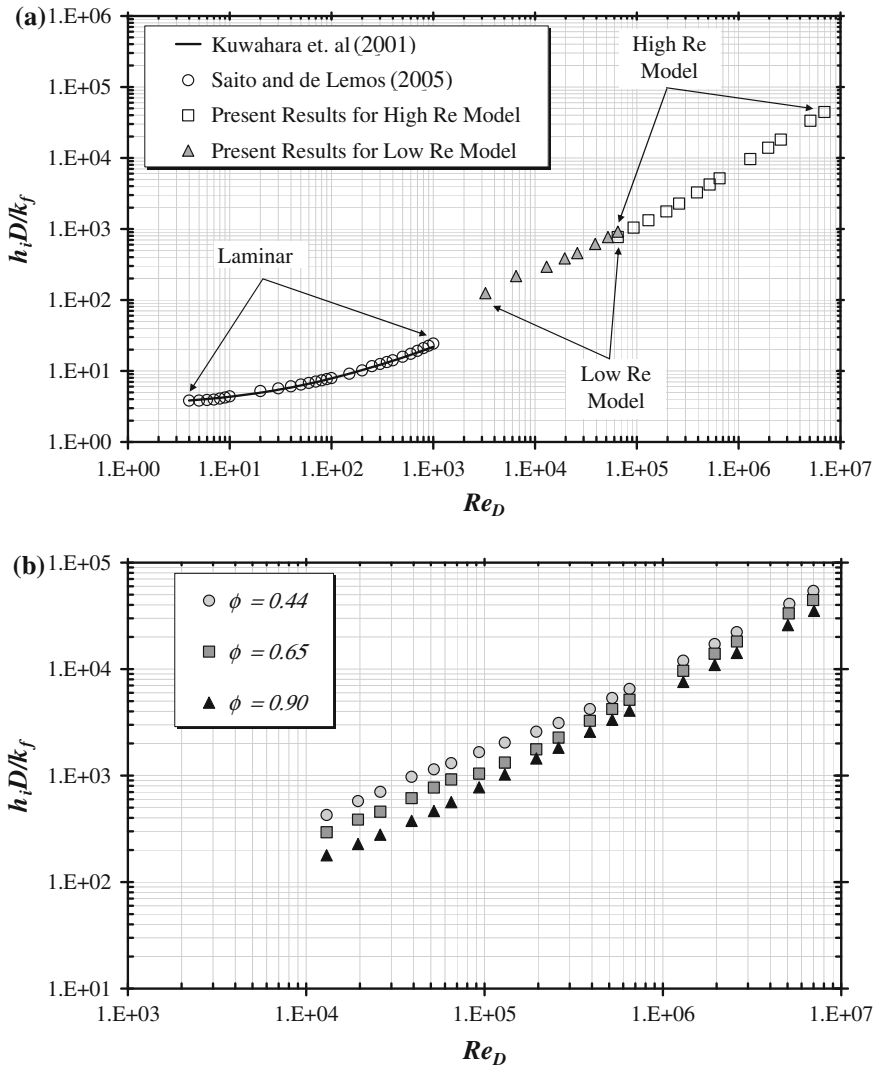


Fig. 2.3 Results for unit cell: **a** Effect of Re_D on h_i for $Pr = 1$ and $\phi = 0.65$, **b** Effect of porosity on h_i for $Pr = 1$

Equation (2.57), which gives the heat transfer coefficient for turbulent flow, is compared with numerical results obtained with Low and High Re models. Such comparison is presented in Fig. 2.4b, which also shows computations using correlations given by Eqs. (2.45) and (2.46) by Wakao et al. [14] and Zhukauskas [18], respectively. The agreement between the present correlation, other correlations in the literature and the numerical simulations stimulates further investigation on this

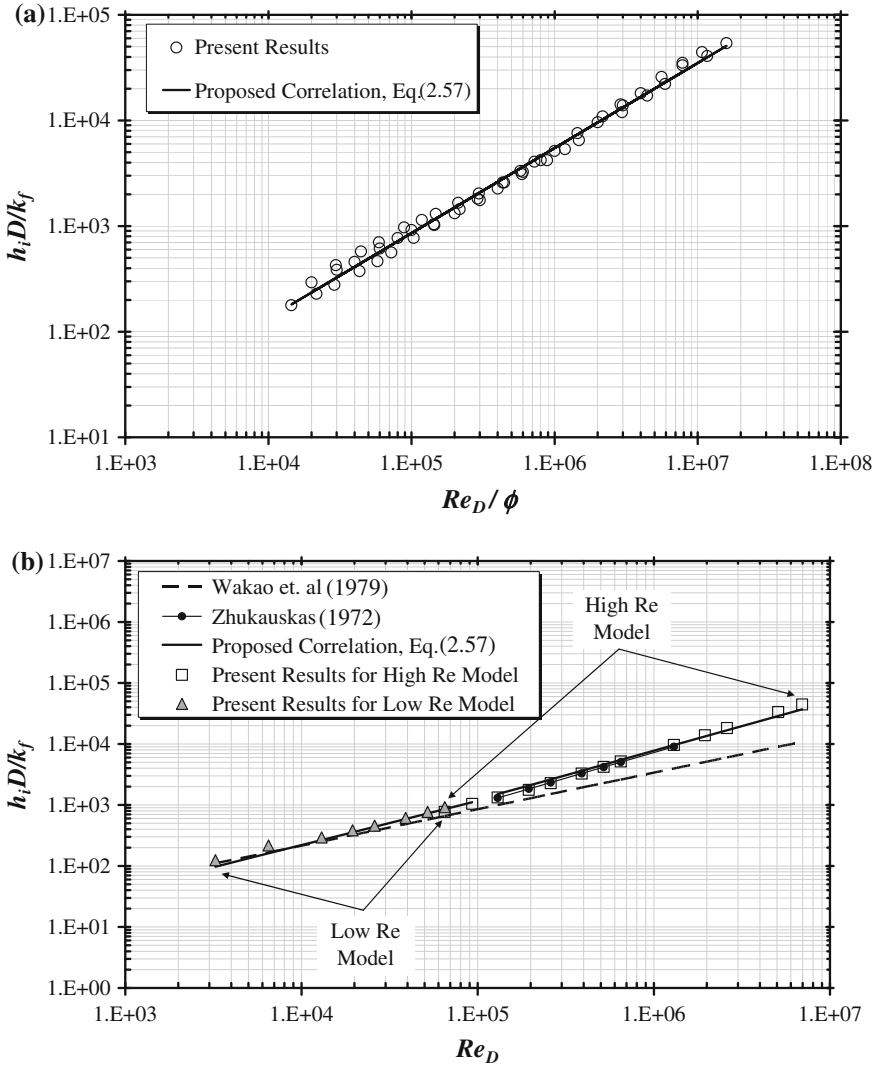


Fig. 2.4 Comparison of the numerical results for unit cell: **a** With proposed correlation Eq. (2.57), **b** With various correlations for $\phi = 0.65$

subject, contributing towards the building of a more general expression for the interfacial heat transfer coefficient for porous media. Table 2.1 compares Eq. (2.57) with other correlations in the literature.

Table 2.1 Correlations for heat transfer coefficient and fluid-to-solid specific area a_i

References	Correlation	Equations	a_i	Flow regime
Wakao et al. [14]	$\frac{h_i D}{k_f} = 2 + 1.1 Re_D^{0.6} Pr^{1/3}$	(2.45)	$\frac{6(1-\phi)}{D}$	Laminar
Kuwahara et al. [15]	$\frac{h_i D}{k_f} = \left(1 + \frac{4(1-\phi)}{\phi}\right) + \frac{1}{2}(1-\phi)^{1/2} Re_D Pr^{1/3}$	(2.46)	$\frac{4(1-\phi)}{D}$	Laminar
Proposed correlation	$\frac{h_i D}{k_f} = 0.08 \left(\frac{Re_D}{\phi}\right)^{0.8} Pr^{1/3}$	(2.57)	$\frac{4(1-\phi)}{D}$	Turbulent

2.4 Laminar Flow in a Channel

This section presents numerical results with the macroscopic model above. The problem considered here is flow through a two-dimensional channel completely filled with a fixed porous substrate, as shown in Fig. 1.3a. Boundary conditions and periodic constraints for turbulent flows in porous media are similar to those applied to clear channel flow.

2.4.1 Non-dimensional Parameters

The longitudinal Nusselt number is calculated for both the fluid and solid phases and is defined as [19],

$$\text{Fluid phase Nusselt number: } Nu_f = -\frac{2H}{T_w - T_{mf}} \left(\frac{\partial \langle T_f \rangle^i}{\partial y} \right), \quad (2.58)$$

$$\text{Solid phase Nusselt number: } Nu_s = -\frac{2H}{T_w - T_{ms}} \left(\frac{\partial \langle T_s \rangle^i}{\partial y} \right), \quad (2.59)$$

where T_{mf} and T_{ms} are the average temperature of the fluid and the solid phase, respectively, and are defined as follows;

$$T_{mf} = \frac{\int u T_f dy}{u_B H}, u_B = \frac{\int u dy}{H}, T_{ms} = \frac{\int T_s dy}{H}, \quad (2.60)$$

The solid phase Nusselt number, Nu_s , was proposed by [19] and refers to a non-dimensional temperature gradient for the solid phase at the wall. This concept has also been applied in reference [20] for laminar flows.

Non-dimensional local and cross-section averaged temperatures, for both phases, are defined as,

$$\theta_{(sf)} = \frac{T_w - T_{(sf)}}{T_w - T_{inlet_{(s,f)}}} \quad (2.61)$$

$$\Theta_{(sf)} = \frac{T_{m_{(sf)}} - T_{inlet_f}}{T_{inlet_s} - T_{inlet_f}}, \quad (2.62)$$

2.4.2 Numerical Method and Boundary Conditions

As before, the numerical method used to discretize the flow and energy equations was the Control Volume approach and the SIMPLE method of Patankar [17] was applied to relax the systems of algebraic equations. For convergence, the normalized residue was set to be lower than 10^{-9} . Boundary conditions are given by:

$$\text{On the solid walls: } \langle \mathbf{u} \rangle^i = 0, \langle T_s \rangle^i = \langle T_f \rangle^i = T_w, \quad (2.63)$$

$$\text{On the entrance: } \mathbf{u}_D = \mathbf{u}_{inlet}, \langle T_s \rangle^i = \langle T_f \rangle^i = T_{inlet}, \quad (2.64)$$

2.4.3 Local Nusselt Numbers

The effect of the Reynolds number is shown in Fig. 2.5 compared with similar computations by Alazmi and Vafai [19]. The Reynolds number is found to have a substantial effect on the development length for Nu along the channel. Figure 2.5c seems to indicate that for lower Reynolds number, the thermal equilibrium condition is achieved faster than for higher Reynolds number cases. Both solid and fluid temperatures reach an equilibrium value along X , decreasing the Nu difference along the channel.

Figure 2.6 shows the effect of porosity on Nusselt for both phases. It is observed from Fig. 2.6a, b that the lower the porosity, the smaller the differences between the present results and those by Alazmi and Vafai [19]. For thermally developed flow and low porosity, both sets of results are closer to each other. Also, the higher the porosity, the higher the Nu number. High porosity condition means a lower interfacial area a_i , reducing the exchange of energy between phases, leading ultimately to higher values of Nu . Figure 2.6c presents similar results in each phase for the entrance region of parallel plates.

The particle diameter, D , is directly related to the interfacial area a_i and appears in the expressions for h_i . Low values for D are associated with high interfacial areas and high interfacial film coefficients. As such, for the same porosity smaller particle

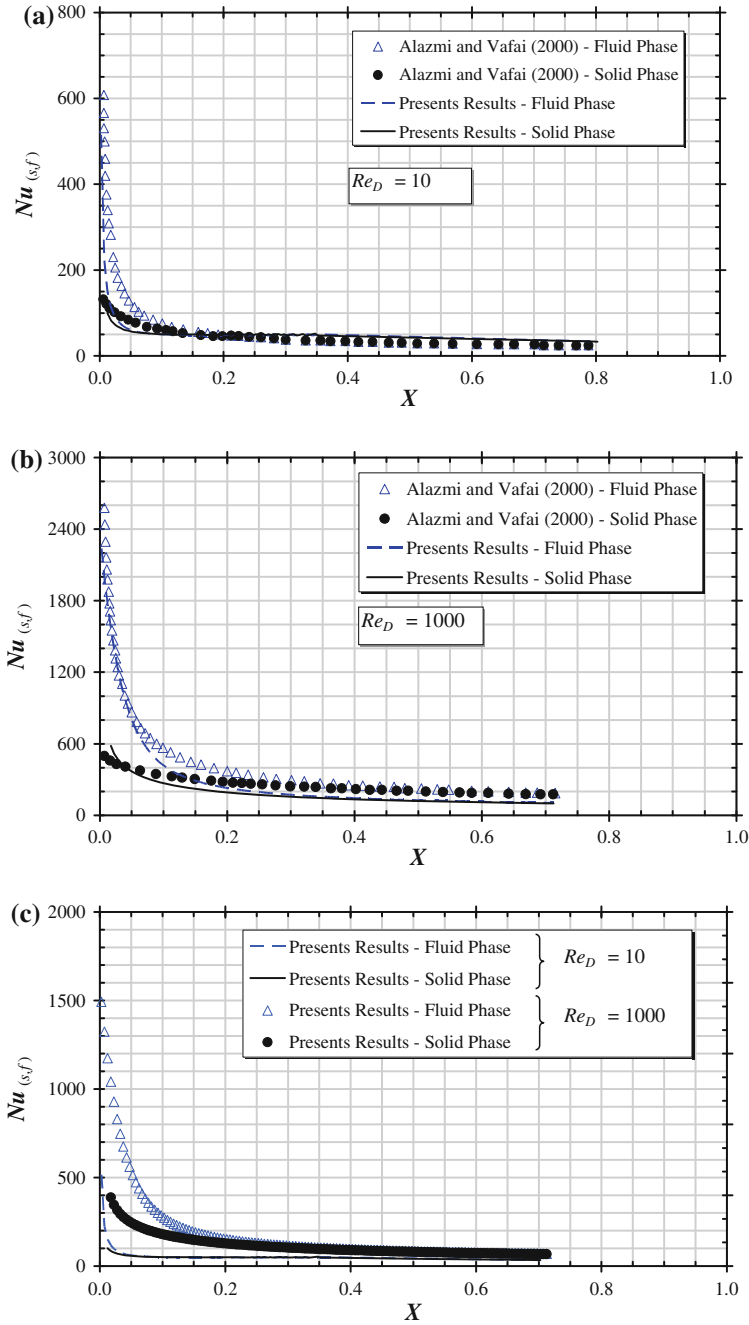


Fig. 2.5 Effect of Re on longitudinal Nusselt number. $Da = 10^{-4}$; $\phi = 0.6$; $D/H = 5.2 \times 10^{-2}$; $k_s/k_f = 25$; **a** $Re_D = 10$, **b** $Re_D = 1000$, **c** Both Re , present results

diameters promote thermal equilibrium between phases by increasing the area of contact between the solid and the fluid. On the other hand, larger particle diameters tend to impair thermal equilibrium between phases, as seen in Fig. 2.7a, b. Figure 2.7c shows the difference between each phase for distinct values of D and shows that thermal equilibrium is reached faster for smaller particle diameters. Also shown is that the larger particle diameters impair thermal equilibrium, affecting temperature distributions and leading to lower Nu numbers for both phases.

Figure 2.8 shows the effect of thermal conductivity ratio on Nu . As seen in Fig. 2.8a, b, a lower conductivity ratio enhances thermal equilibrium by reducing temperature differences between phases. Figure 2.8c presents a comparison of Nusselt numbers indicating that for a high conductivity ratio, impairment on the exchange of energy between phases affects local temperature values, ultimately reducing corresponding Nusselt numbers.

Finally, Fig. 2.9 shows a comparison of present results and those by Wakao et al. [14] and Kuwahara et al. [15] correlations in addition to results by Alazmi and Vafai [19]. It is clearly seen from Fig. 2.9 that a reasonable agreement is found between the predictions, except for the Kuwahara correlation [15] for the fluid phase Nusselt number, which is slightly higher. This discrepancy could be explained due to the fact that predictions by Alazmi and Vafai [19] were obtained with Wakao correlation [14], which is calculated considering a_i based on circular rods instead of square rods.

2.5 Turbulent Flow in a Channel

Results below were obtained after extensive testing on grid size independence and search for optimal relaxation parameters. Due to lack of space here, the interest reader is referred to previous work where such studies are presented in detail [20–22].

Also, for turbulent flow ($Re_D = 5 \times 10^4$), a sensitive analysis on the value of h_i is performed in order to evaluate the correctness of code programming. Figure 2.10 shows results for the cross-section averaged temperatures for both the solid and fluid phases. As in the case of laminar flow, a nominal value for h_i is employed in Fig. 2.10b and compared with artificially increased (Fig. 2.10a) and reduced (Fig. 2.10c) values of the interfacial film coefficient. Also for turbulent flow, shorter (Fig. 2.10a) and larger (Fig. 2.10c) developing lengths correspond to higher and lower values for h_i , respectively, indicating that physically realistic results for temperatures are obtained.

Next, the effect of introducing K_{disp} in the calculations for turbulent flow is presented in Figure Fig. 2.11, for the conditions $Da = 10^{-4}$, $Re_D = 5 \times 10^4$, $D/H = 1.03 \times 10^{-1}$, $k_s/k_f = 25$ and $\phi = 0.6$. The differences between the solid and fluid phase temperature profiles are greater when thermal dispersion is

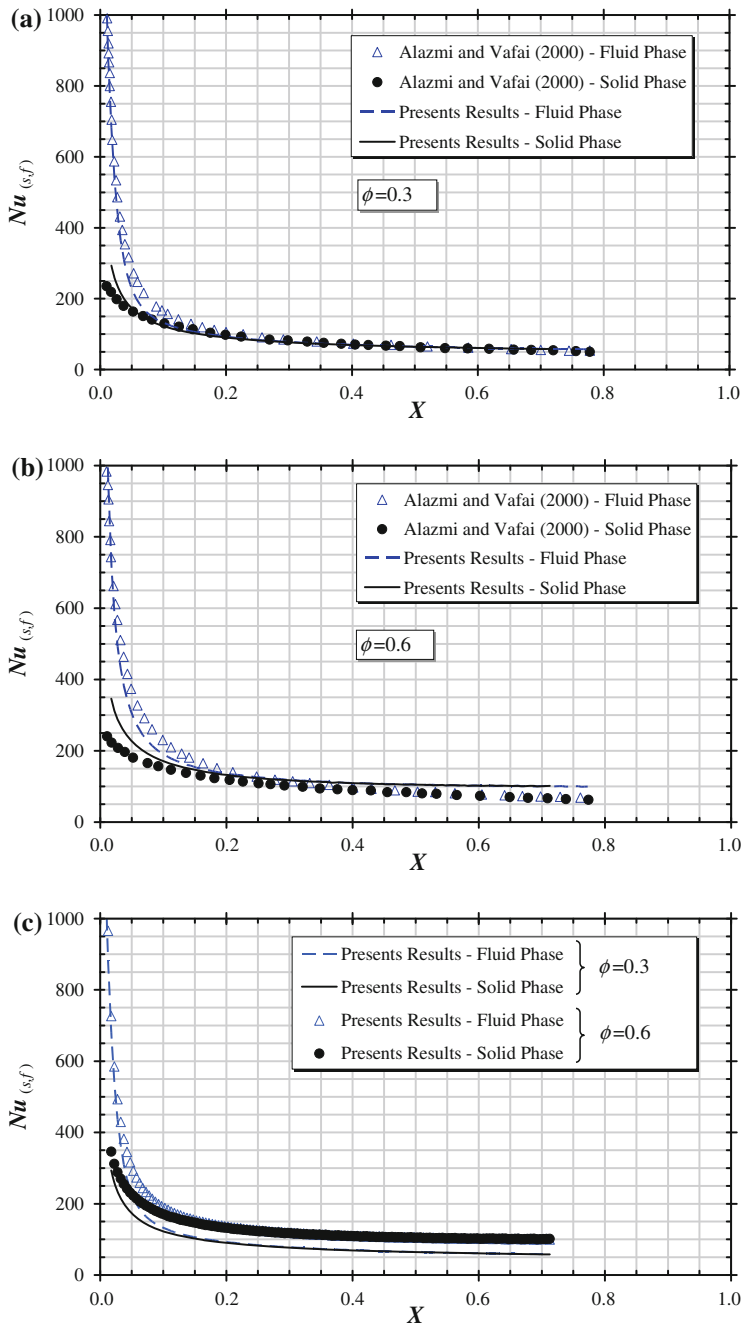


Fig. 2.6 Effect of porosity on longitudinal Nusselt number, $Re_D = 100$, $D/H = 5.2 \times 10^{-2}$, $k_s/k_f = 25$: **a** $\phi = 0.3$, **b** $\phi = 0.6$, **c** Both porosities, present results

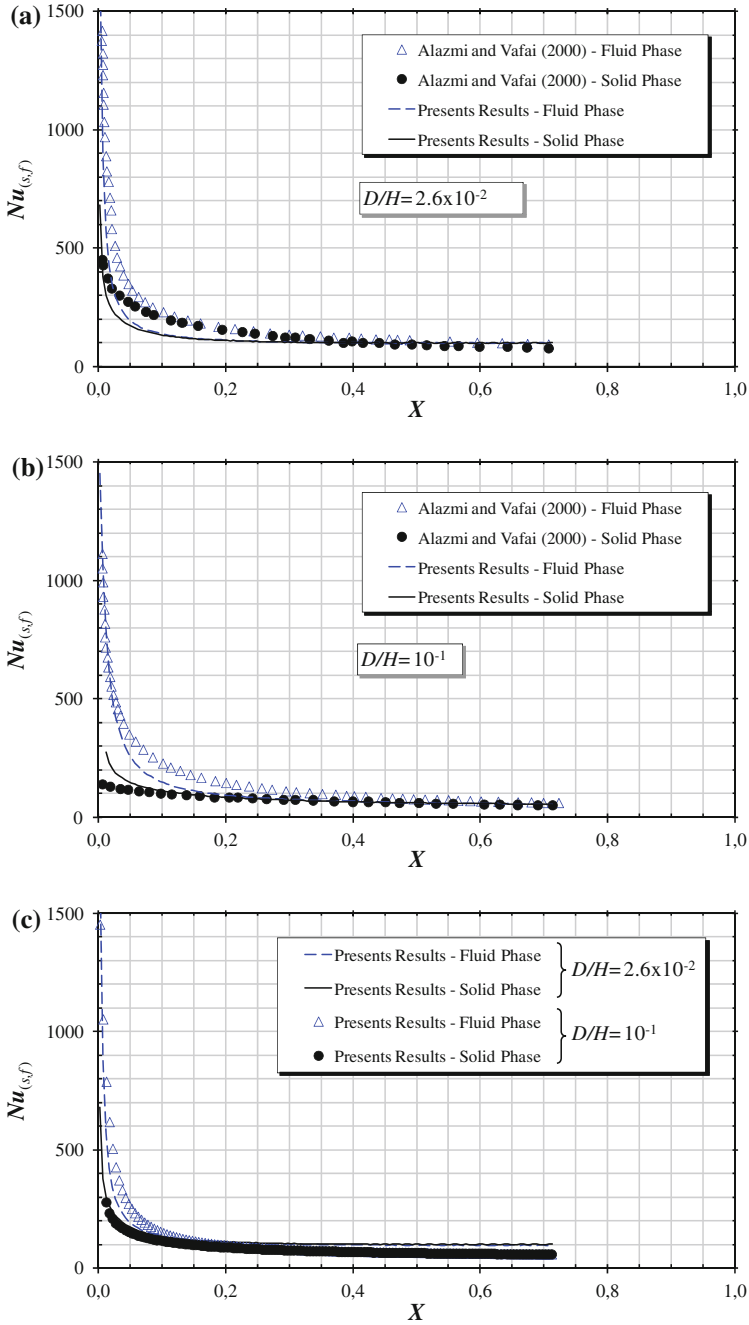


Fig. 2.7 Effect of D on longitudinal Nusselt number. $Da = 10^{-4}$; $Re_D = 100$; $\phi = 0.6$; $k_s/k_f = 25$;
a $D/H = 2.6 \times 10^{-2}$, **b** $D/H = 10^{-1}$, **c** Both D/H ratios, present results

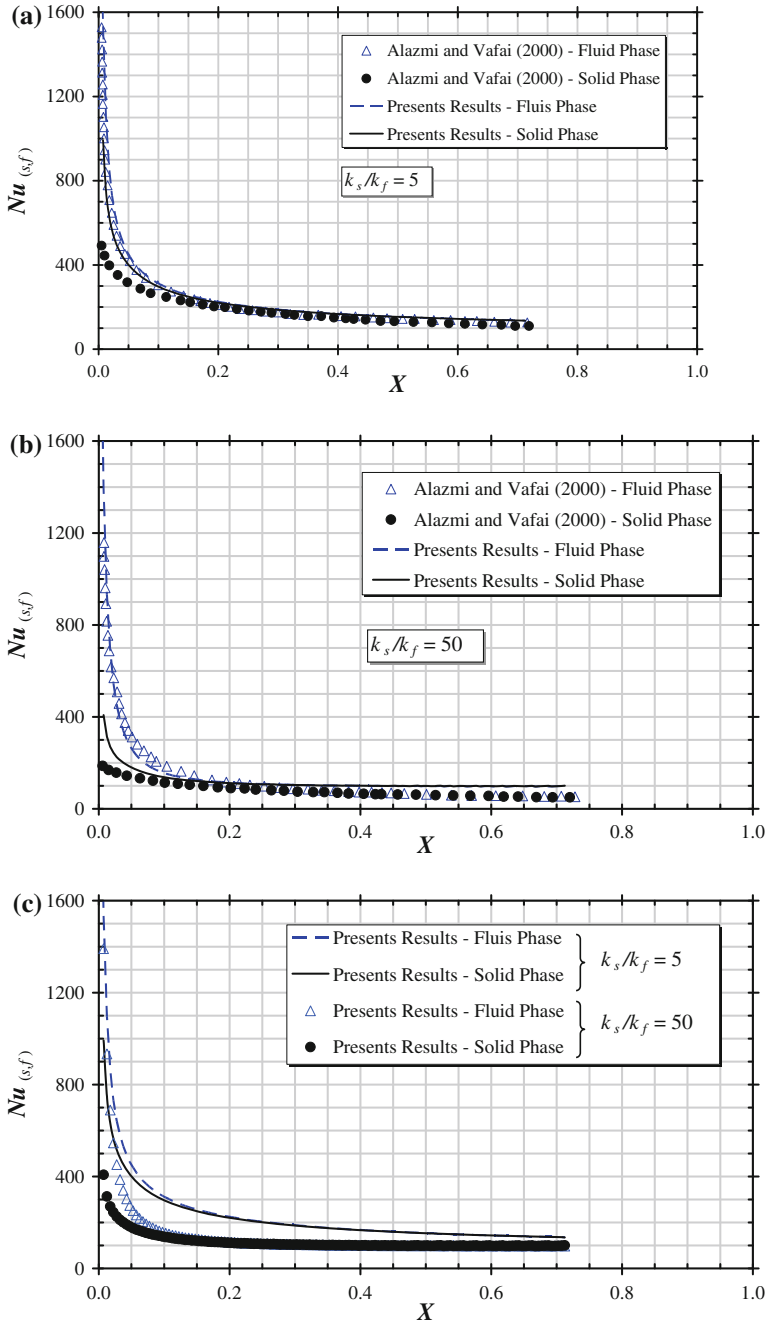


Fig. 2.8 Effect of solid-to-fluid thermal conductivity ratio on longitudinal Nusselt number. $Da = 10^{-4}$; $Re_D = 100$; $\phi = 0.6$; $D/H = 5.2 \times 10^{-2}$; **a** $k_s/k_f = 5$, **b** $k_s/k_f = 50$, **c** Both k_s/k_f ratios, present results

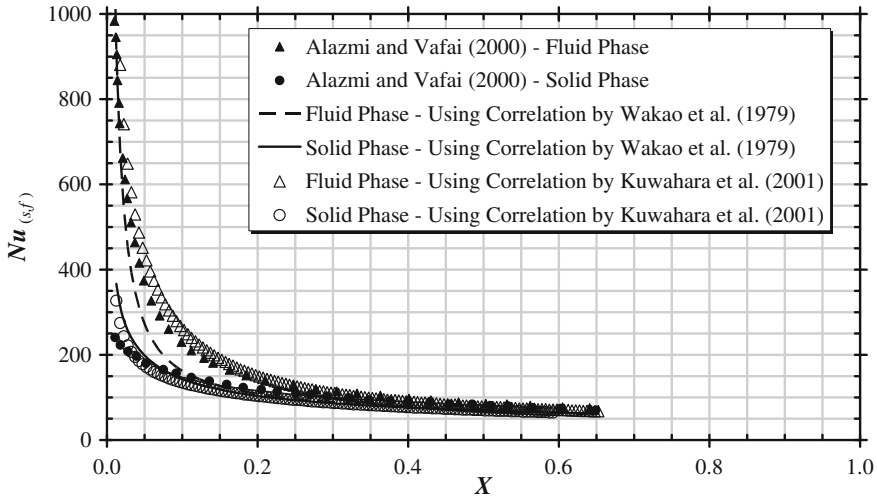


Fig. 2.9 Comparison between present results with various correlations and Alazmi and Vafai (2000) results. $Da = 10^{-4}$; $Re_D = 100$; $\phi = 0.6$; $D/H = 5.2 \times 10^{-2}$; $k_s/k_f = 25$

incorporated in the macroscopic model, particularly in the near wall region ($Y < 0.1$), which embraces the boundary layer that is much thinner than for laminar flows cases. Therefore, here also the role of the additional mechanism of dispersion is to promote diffusion across the cross section of the channel, leading to flatter $\langle \bar{T}_f \rangle^i$ profiles and larger temperature differences from corresponding local values of $\langle \bar{T}_s \rangle^i$. Effects of Reynolds number, Re_D , porosity, ϕ , non-dimensional particle diameter, D/L , and solid-to-fluid thermal conductivity, k_s/k_f , on temperature behavior are shown next.

Figure 2.12 shows the effect of the Reynolds number and boundary condition on Nu . One can note in the figure that an increase in Re_D results in an increase in Nusselt, for all cases, as expected. For high values of Re_D , Nu_f and Nu_s are closer to each other when compared with similar computations for $Re_D = 10^5$ (Fig. 2.12b). Figure 2.12c shows a comparison of all cases and indicates that Nu_f attains higher values than Nu_s , along the flow direction.

In Fig. 2.13a, b the effect of porosity ϕ on Nu is presented. An increase in porosity causes the solid phase Nusselt number to decrease whereas Nu_f is augmented, for both boundary condition types. Increase in this difference for low porosity medium could be explained by noting that a higher ϕ gives a lower h_i , according to Eq. (2.57), as well as a lower a_i , as seen in Table 2.1. Their product, $h_i a_i$, is proportional to the heat transfer between phases, as shown by the two energy Eqs. (2.36) and (2.37). Consequently, a high porosity medium will have the intensity of energy transfer between phases reduced, reflecting in the temperature fields and, ultimately, on the calculated Nu values.

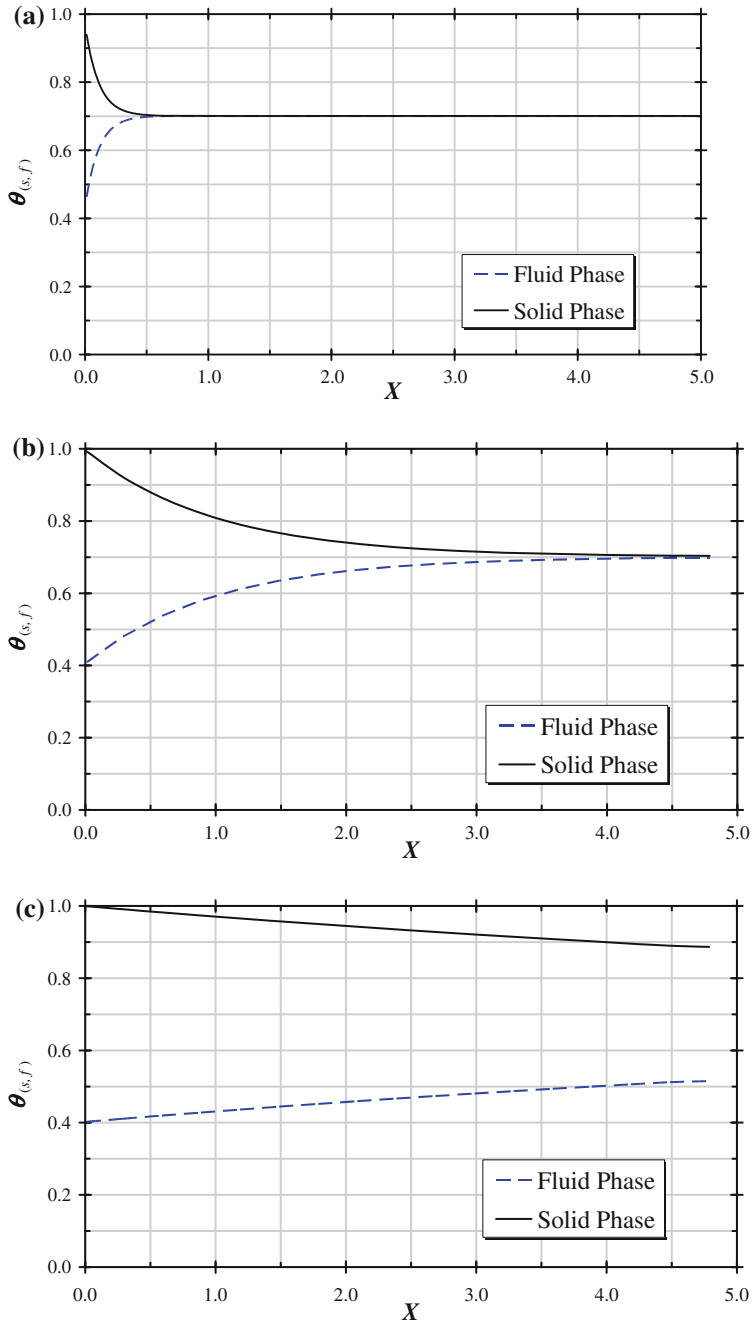


Fig. 2.10 Fluid and solid cross-sectional averaged temperatures along the flow, $Da = 10^{-4}$; $Re_D = 5 \times 10^4$, $\phi = 0.6$; $D/H = 1.03 \times 10^{-1}$; $k_s/k_f = 25$: **a** $h_{eff} = 10h_i$, **b** $h_{eff} = h_i$, **c** $h_{eff} = 0.1h_i$

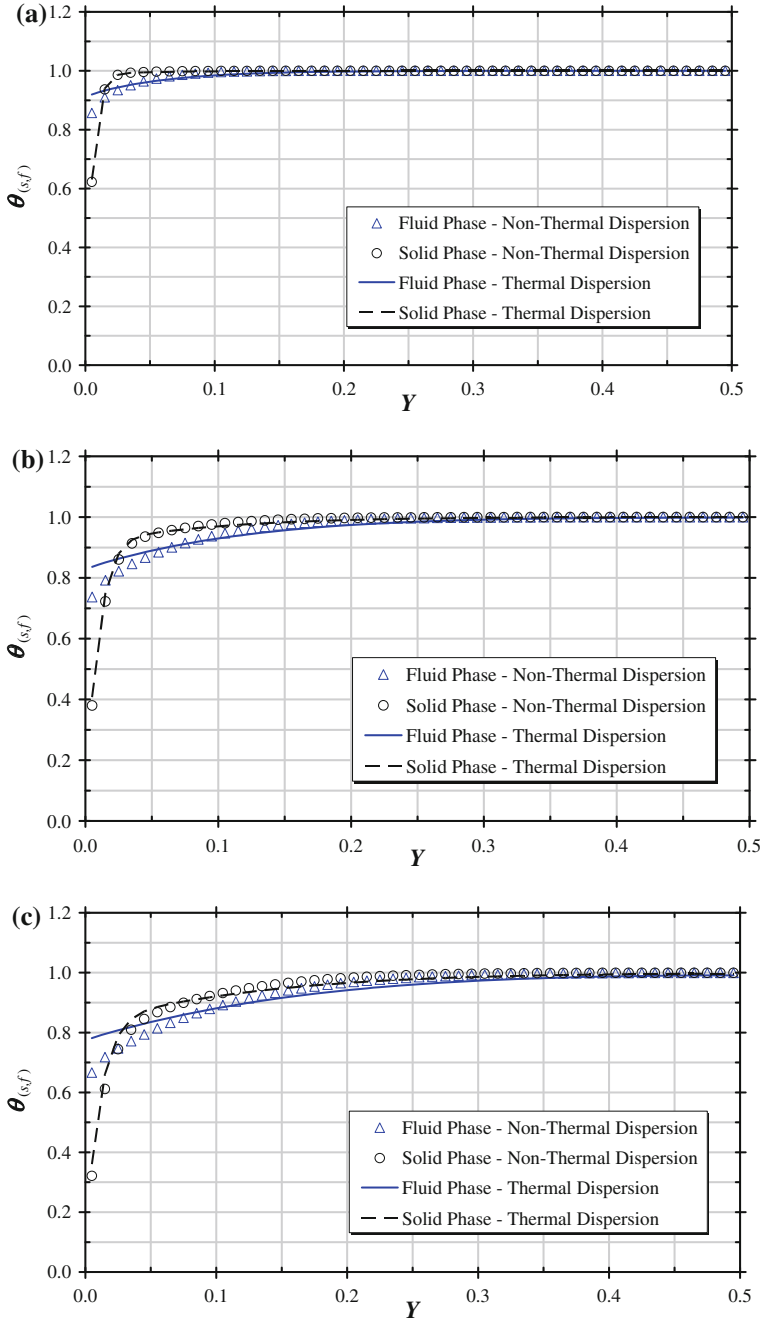


Fig. 2.11 Effect of thermal dispersion on local non-dimensional temperatures, $Da = 10^{-4}$, $Re_D = 5 \times 10^4$, $\phi = 0.6$; $D/H = 1.03 \times 10^{-1}$, $k_s/k_f = 25$: **a** $X = 0.1$, **b** $X = 0.5$, **c** $X = 1$

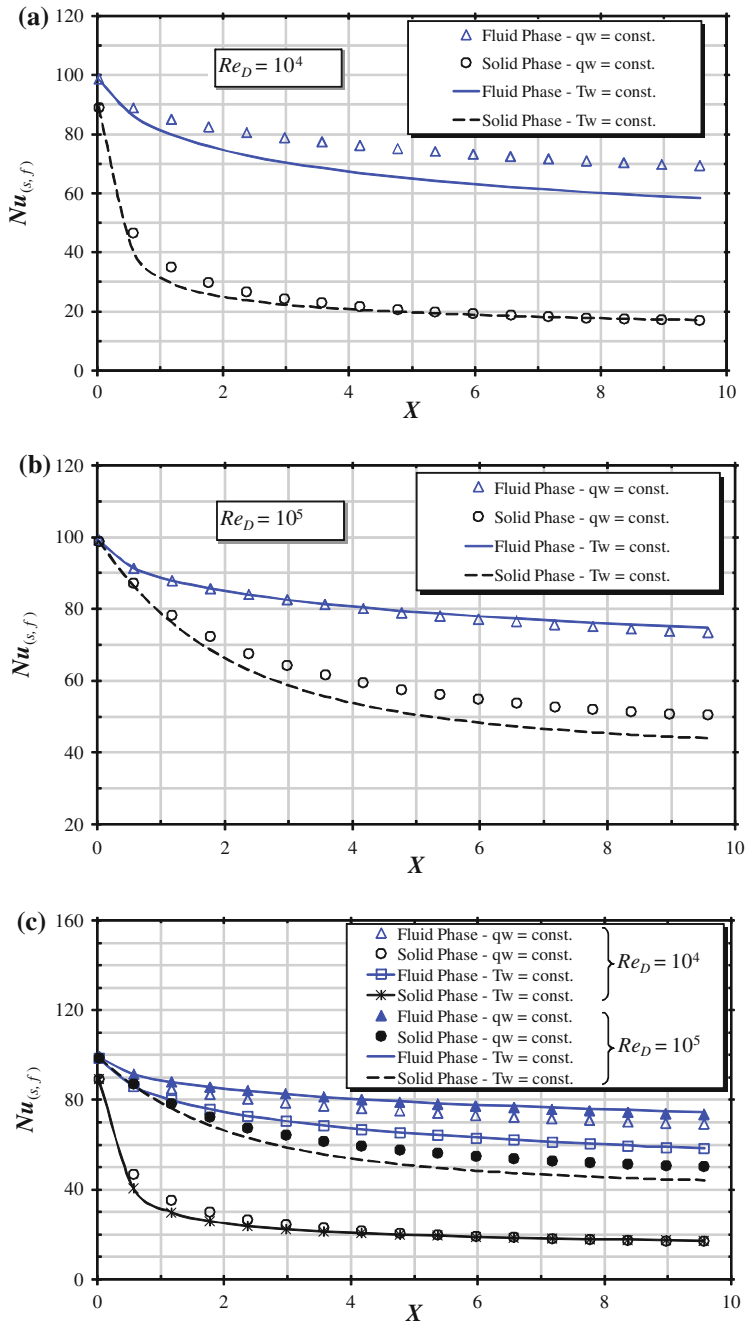


Fig. 2.12 Effect of Re_D on Nu for turbulent flow, $Da = 10^{-4}$, $\phi = 0.6$, $D/H = 1.03 \times 10^{-1}$, $k_s/k_f = 25$: **a** $Re_D = 10^4$, **b** $Re_D = 10^5$, **c** Both Re_D

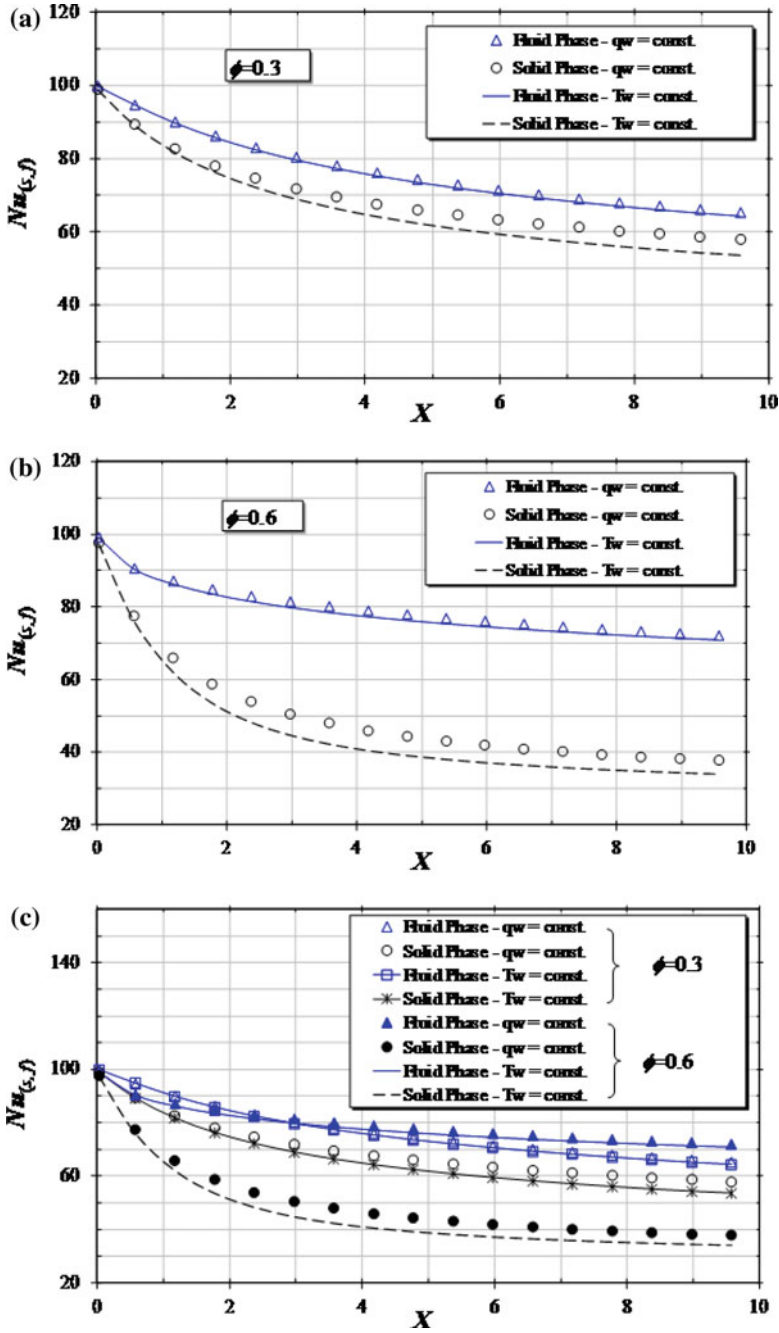


Fig. 2.13 Effect of ϕ on Nu for turbulent flow, $Da = 10^{-4}$; $Re_D = 5 \times 10^4$; $D/L = 1.03 \times 10^{-2}$; $k_s/k_f = 25$; **a** $\phi = 0.3$, **b** $\phi = 0.6$, **c** Both ϕ

Figure 2.14 shows the effect of the non-dimensional particle diameter D/L on Nusselt, for a fixed porosity. In general, an increase in the particle diameter D/L results in an increase in Nusselt, for both phases and both boundary condition types (Fig. 2.14a, b). When porosity is constant and the thermal dispersion effects are omitted, the particle diameter only affects h_i and a_i [see Eq. (2.57) and Table 2.1]. A reduced value for D/L with a constant ϕ increases the interstitial area, promoting the exchange of energy between phases, leading to a reduction of the temperature gradients in the wall region, which ultimately reflects on the Nu values. Figure 2.14c compiles such findings and shows for turbulent flow, small differences on Nu prevail in spite of the boundary condition type used.

Effects of the ratio k_s/k_f is presented in Fig. 2.15. All computations made so far were obtained with $k_s/k_f = 25$ and when one compares Fig. 2.15a, b, one can note that the lower such ratio, the closer are the values for the Nusselt numbers, regardless of the boundary condition used. When the fluid and the solid conduct heat at rates of the same order, their temperatures levels do not differ much, with reflection on the proximity of corresponding Nusselt numbers. Further, differences between the Nusselt numbers for $q_w = \text{const.}$ and $T_w = \text{const.}$ are reduced for the solid, when k_s/k_f is large, and increased for the fluid, for small values of k_s/k_f (Fig. 2.15c).

2.6 Chapter Summary

A computational procedure for determining the convective coefficient of heat exchange between the porous substrate and the working fluid for a porous medium was detailed. As a preliminary result, macroscopically uniform laminar and turbulent flow through a periodic cell of isothermal square rods was computed, considering periodical velocity and temperature fields. Quantitative agreement was obtained when comparing laminar results herein with simulations by Kuwahara et al. [15]. For turbulent flows, Low and High Reynolds turbulence models were employed in order to obtain the interfacial heat transfer coefficient. A correlation was then proposed for such coefficient. Further work will be carried out in order to simulate fully turbulent flow and heat transfer in a porous medium formed by arrays of elliptic, cylindrical and transverse elliptic rods, displaced in in-line as well as staggered arrangements. Ultimately, it is expected that a more general correlation for h_i be obtained to be used in conjunction with macroscopic two-energy equation models.

Also, fully developed forced convection in a porous channel bounded by parallel plates based on a two-energy equation model is analyzed. Details are presented for determining the temperature profile and Nusselt number for laminar flows in a porous medium. Results simulate the effects of Re , ϕ , D and k_s/k_f on Nu . High Re , low porosities, low particle diameters and low thermal conductivity ratios promote thermal equilibrium between phases, eventually leading to higher values of Nu for

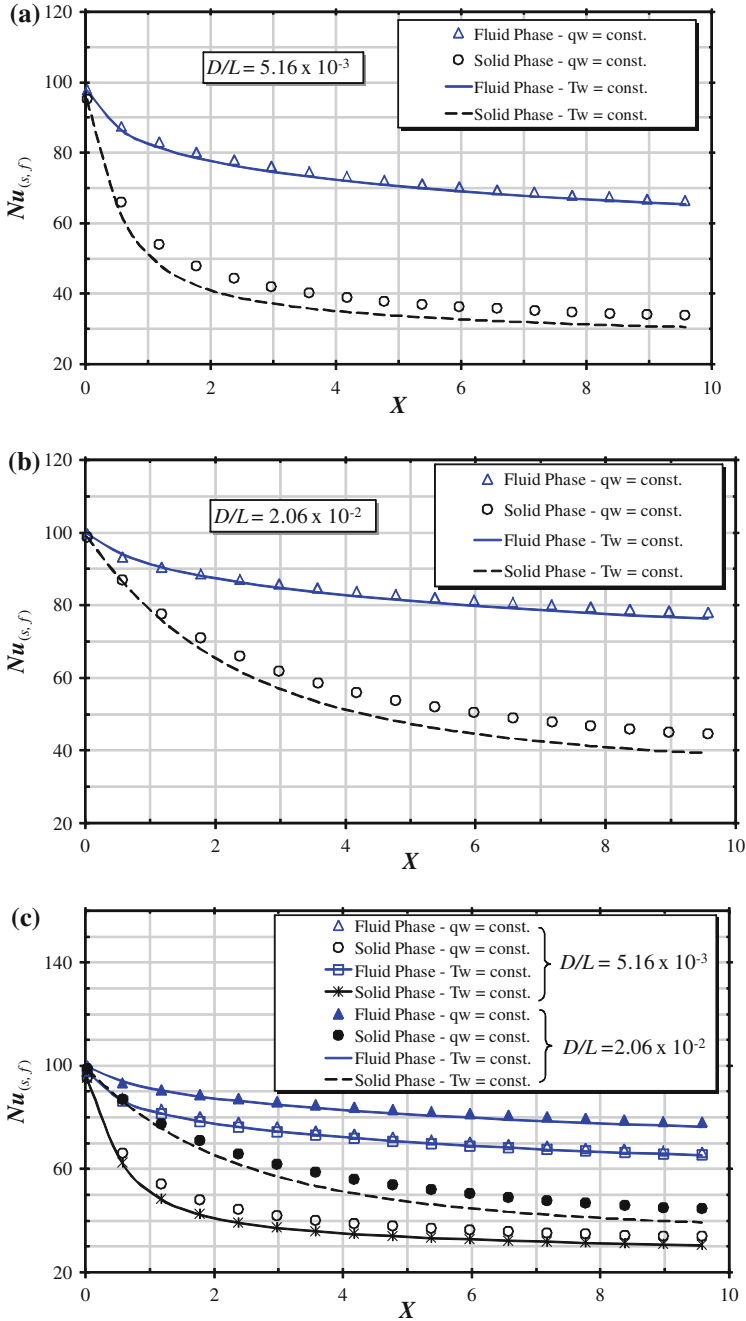


Fig. 2.14 Effect of D/L on Nu for turbulent flow, $Re_D = 5 \times 10^4$; $\phi = 0.6$; $k_s/k_f = 25$:
a $D/L = 5.16 \times 10^{-3}$, **b** $D/L = 2.06 \times 10^{-2}$, **c** Both D/L

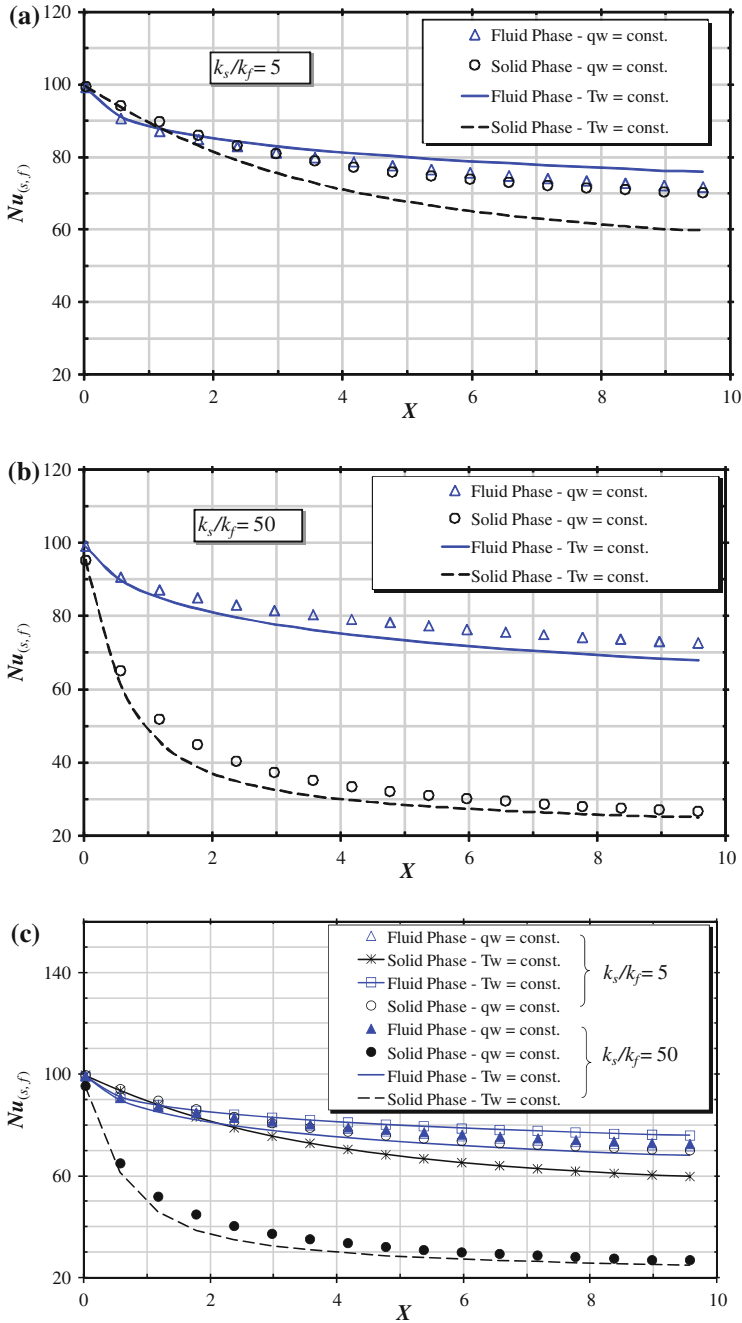


Fig. 2.15 Effect of k_s/k_f on Nu for turbulent flow, $Da = 10^{-4}$, $Re_D = 5 \times 10^4$, $\phi = 0.6$, $D/H = 1.03 \times 10^{-1}$: **a** $k_s/k_f = 5$, **b** $k_s/k_f = 50$

both the fluid and the solid. Further work will be carried out in order to simulate fully turbulent flow and heat transfer in a porous medium with the macroscopic two-energy equation model.

Further, this chapter also investigated the behavior of a two-energy equation model to simulate flow and heat transfer in a porous bed. Effects of thermal dispersion, Reynolds number, particle diameter, porosity and solid-to-fluid thermal conductivity ratio were investigated. The following conclusions were observed:

- (1) For laminar flow, the thermal dispersion mechanism promotes energy exchange in the fluid phase, leading to larger local temperature differences when the solid and the fluid temperature are compared along the channel cross-section, particularly at the entry region,
- (2) For turbulent flow, the effect of including the thermal dispersion mechanism is concentrated in the region close to the wall, within the boundary layer, where such temperature differences are pronounced,
- (3) Increase in Re number causes values for Nu of both phases to increase and to approach each other,
- (4) An increase in porosity causes the solid phase Nusselt number to decrease whereas Nu_f is augmented, for both boundary condition types. A high porosity medium will have the intensity of energy transfer between phases reduced, reflecting in the temperature fields and, ultimately, on the calculated Nu values.
- (5) A reduced value for D/L with a constant porosity increases the interstitial area, promoting the exchange of energy between phases, leading to a reduction of the temperature gradients in the wall region. In general, an increase in the particle diameter results in an increase in Nusselt, for both phases and both boundary conditions.
- (6) The thermal conductivity ratio k_s/k_f causes the most effect on Nusselt numbers, and the greater the ratio, the most wider apart are Nu_s and Nu_f , with a reduction of Nusselt for the solid phase.

References

1. Schumann TEW (1929) Heat transfer: liquid flowing through a porous prism. *J Franklin Inst* 208:405–416
2. Kaviany M (1995) Principles of heat transfer in porous media, 2nd edn. Springer, New York
3. Quintard M, Kaviany M, Whitaker S (1997) Two-medium treatment of heat transfer in porous media: numerical results for effective properties. *Adv Water Resour* 20:77–94
4. Ochoa-Tapia JA, Whitaker S (1997) Heat transfer at the boundary between a porous medium and a homogeneous fluid. *Int J Heat Mass Transf* 40:2691–2707
5. Saito MB, de Lemos MJS (2005) Interfacial heat transfer coefficient for non-equilibrium convective transport in porous media. *Int Comm Heat Mass Transf* 32(5):667–677

6. de Lemos MJS, Rocamora FD (2002) Turbulent transport modeling for heated flow in rigid porous media. In: Proceedings of the twelfth international heat transfer conference, Grenoble, France, 18–23 Aug 2002, pp 791–795
7. Launder BE, Spalding DB (1974) The numerical computation of turbulent flows. *Comp Meth Appl Mech Eng* 3:269–289
8. Pedras MHJ, de Lemos MJS (2000) On the definition of turbulent kinetic energy for flow in porous media. *Int Comm Heat Mass Transf* 27(2):211–220
9. Pedras MHJ, de Lemos MJS (2001) Simulation of turbulent flow in porous media using a spatially periodic array and a low-Re two-equation closure. *Numer Heat Transf, Part A Appl* 39(1):35–59
10. Pedras MHJ, de Lemos MJS (2003) Computation of turbulent flow in porous media using a Low Reynolds $k - \varepsilon$ model and an infinite array of transversally-displaced elliptic rods, *Numer Heat Transf Part A, Appl* 43(6):585–602
11. Gray WG, Lee PCY (1977) On the theorems for local volume averaging of multiphase system. *Int J Multiph Flow* 3:333–340
12. Slattery JC (1967) Flow of viscoelastic fluids through porous media, *A I Ch E J* 13:1066–1071
13. Kuwahara F, Nakayama A, Koyama H (1996) A numerical study of thermal dispersion in porous media. *J Heat Transfer* 118:756–761
14. Wakao N, Kaguei S, Funazkri T (1979) Effect of fluid dispersion coefficients on particle-to-fluid heat transfer coefficients in packed bed. *Chem Eng Sci* 34:325–336
15. Kuwahara F, Shiota M, Nakayama A (2001) A numerical study of interfacial convective heat transfer coefficient in two-energy equation model for convection in porous media. *Int J Heat Mass Transf* 44:1153–1159
16. Nakayama A, Kuwahara F, Sugiyama M, Xu G (2001) A two-energy equation model for conduction and convection in porous media. *Int J Heat Mass Transf* 44:4375–4379
17. Patankar SV (1980) Numerical heat transfer and fluid flow. Hemisphere, Washington, DC
18. Zhukauskas A (1972) Heat transfer from tubes in cross flow, advances in heat transfer, 8. Academic Press, New York
19. Alazmi B, Vafai K (2000) Analysis of variants within the porous media transport models. *J Heat Transf* 122:303–326
20. Saito MB, de Lemos MJS (2009) Laminar heat transfer in a porous channel simulated with a two-energy equation model. *Int Commun Heat Mass Transf* 36:1002–1007
21. Rocamora FD Jr, de Lemos MJS (2000) Analysis of convective heat transfer of turbulent flow in saturated porous media. *Int Comm Heat Mass Transf* 27(6):825–834
22. de Lemos MJS, Silva RA (2006) Turbulent flow over a layer of a highly permeable medium simulated with a diffusion-jump model for the interface. *Int J Heat Mass Transf* 49(3–4):546–556

Thermal Non-Equilibrium in Heterogeneous Media

de Lemos, M.J.S.

2016, XXV, 108 p. 31 illus., 5 illus. in color., Softcover

ISBN: 978-3-319-14665-2